FRONTIERS OF PHYSICS

RESEARCH ARTICLE
Volume 19 / Issue 4 / 43203 / 2024

Tunable near-infrared light emission from layered TiS_3 nanoribbons

Junrong Zhang[1,2], Cheng Chen[1,2], Yanming Wang[1,2], Yang Lu[1,2], Honghong Li[3], Xingang Hou[2], Yaning Liang[2,4], Long Fang[2,5], Du Xiang[3,†], Kai Zhang[1,2,‡], Junyong Wang[1,2,§]

1 School of Nano-Tech and Nano-Bionics, University of Science and Technology of China, Hefei 230026, China
2 CAS Key Laboratory of Nanophotonic Materials and Devices & Key Laboratory of Nanodevices and Applications, i-Lab, Suzhou Institute of Nano-Tech and Nano-Bionics (SINANO), Chinese Academy of Sciences, Suzhou 215123, China
3 Frontier Institute of Chip and System, Fudan University, Shanghai 200438, China
4 School of Materials Science and Engineering, Shanghai University, Shanghai 200444, China
5 College of Energy & Power Engineering, Inner Mongolia University of Technology, Hohhot 010051, China
Corresponding authors. E-mail: †xiang_du@fudan.edu.cn, ‡kzhang2015@sinano.ac.cn, §jywang2022@sinano.ac.cn
Received October 20, 2023; accepted November 30, 2023

ABSTRACT

The low-dimensional light source shows promise in photonic integrated circuits. Stable layered van der Waals material that exhibits luminescence in the near-infrared optical communication waveband is an essential component in on-chip light sources. Herein, the tunable near-infrared photoluminescence (PL) of the air-stable layered titanium trisulfide (TiS_3) is reported. Compared with iodine particles as a transport agent, TiS_3 grown by chemical vapor transport using sulfur powder as a transport agent has fewer sulfur vacancies, which increases the luminescence intensity by an order of magnitude. The PL emission wavelength can be regulated in the near-infrared regime by thickness control. In addition, we observed an interesting anisotropic strain response of PL in layered TiS_3 nanoribbon: a blue shift of PL was achieved when the uniaxial tensile strain was applied along the *b*-axis, while a negligible shift was observed when the strain was applied along the *a*-axis. Our work reveals the tunable near-infrared luminescent properties of TiS_3 nanoribbons, suggesting their potential applications as near-infrared light sources in photonic integrated circuits.

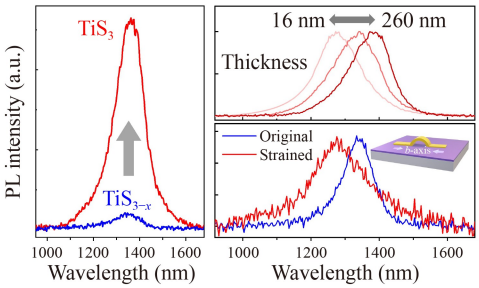

Keywords titanium trisulfide, near-infrared luminescence, S-vacancy, tunability, strain engineering

1 Introduction

Photonic integrated circuits offer new opportunities for faster and energy-efficient communication and computing systems [1–6]. A low-dimensional light source, which has the advantages of miniaturization and compatibility, is a competitive optical component in photonic integrated circuits. In the last decade, light sources based on layered van der Waals materials have been reported [7, 8], such as transition metal dichalcogenides (TMDs) [9–16] and black phosphorus (BP) [17–19]. The semiconducting TMDs in monolayer form possess a direct

*Special Topic: Surface and Interface of Two-dimensional Materials (Eds.: Lijun Zhang, Dongchen Qi, Ming Yang & Kai Zhang).

Higher Education Press

https://doi.org/10.1007/s11467-023-1376-1

bandgap with typical light emission in the visible waveband. Monolayer $MoTe_2$ exhibits light emission in the near-infrared waveband with a bandgap of ~1.1 eV [20, 21]. However, 2D materials with emissions in the near-infrared communication regime, such as the O and C bands, are limited. Trilayer and tetralayer BP exhibit excitonic emission at around 1280 and 1480 nm, respectively [22]. However, the air instability of BP, especially for the thin layers, hinders its practical application.

As a member of the transition metal trichalcogenides (TMTs), titanium trisulfide (TiS_3) has attracted much attention due to its anisotropy optical and electronic properties resulting from its quasi-one-dimensional (1D) crystal structure [23, 24]. Interestingly, TiS_3 shows a direct bandgap of about 0.9 eV [25–28], lying in the near-infrared communication waveband, which makes it a promising luminescent material for on-chip light sources. However, the studies on the optical emission properties of TiS_3 are limited, which may be hindered by the content of S vacancies and abundant nonradiative recombination process in TiS_3 [29–31]. Therefore, controlling and reducing the sulfur vacancies is of great significance to exploit the luminescent properties of TiS_3. In addition, the regulation of wavelength is desirable for the information application as an intelligent on-chip light source. The van der Waals semiconductors with versatile thickness control and strain engineering offer the opportunity to modulate their band structure and the light emission wavelengths.

Here, we report on the regulation of the light emission intensity and wavelength of TiS_3 in the near-infrared regime. By comparing the transport agent of S powder and iodine granule in the chemical vapor transport (CVT) growth method, we found that the photoluminescence (PL) emission of TiS_3 can be increased by an order of magnitude by changing the transport agent from iodine granule to S powder. Broad PL tunability from 1269 to 1385 nm near the O band in TiS_3 nanoribbon was demonstrated by controlling the flake thicknesses. In addition, by using uniaxial tensile strain, the center wavelength of PL from TiS_3 can be tuned reversibly from 1289 nm to 1342 nm. Interestingly, an anisotropic strain response of PL in TiS_3 nanoribbons has been observed. The tunable light emission from the van der Waals TiS_3 shows potential applications in photonic integrated circuits for optical fiber communication.

2 Experimental section

Materials synthesis. The TiS_3 and TiS_{3-x} bulk crystals were synthesized by the CVT method. For the growth of TiS_3 crystal, Ti powder (Alfa Aesar, 99.99%) and sulfur (S) powder (Alfa Aesar, 99.99%) with a Molar ratio of 1:3.05 were mixed and sealed in a clear quartz ampule under a vacuum of ~10^{-2} Pa, the excess sulfur was considered as transport agents. The quartz ampule was placed in a two-zone tube furnace, slowly heated to 480–620 °C (the temperature corresponds to the cold zone and hot zone of the tube furnace, respectively), and maintained for five days. After the tube furnace was naturally cooled to room temperature, high-quality shiny ribbon-like TiS_3 was obtained in the cold zone. For the growth of TiS_{3-x} crystal, Ti powder (Alfa Aesar, 99.99%) and S powder (Alfa Aesar, 99.99%) with a molar ratio of 1:3 were used as precursors (the total mass was 1 g), and 15 mg of the iodine granule (Alfa Aesar, 99.99%) was used as transport agent, the subsequent growth process was similar to the aforementioned for TiS_3.

Materials characterization. The crystal structure of TiS_3 was characterized by XRD (Bruker, D8 Advance) in the 2θ range of 5°–65°. The thickness of all flakes was characterized using an AFM (Bruker, Dimension ICON). The crystalline quality and chemical composition of TiS_3 were characterized using SEM (Quanta FEG 250) and STEM (Themis Z, operating at 300 kV).

Optical measurement. The Raman spectra and angle-dependent Raman spectra were measured by a micro-Raman system (LABRAM HR) with a 532 nm laser through a 100X objective lens. The optical absorption and optical bandgap were measured by ultraviolet-visible-near infrared (UV–vis-NIR) spectrophotometer (SHIMADZU, UV-1280). Near-infrared μ-PL measurement was carried out on a commercial confocal μ-PL system (Fuxiang, golite solution-PL). A single-mode fiber laser at 532 nm was used to excite the PL of TiS_3 nanoribbon. Angle-dependent near-infrared PL spectra were measured by using an analyzer (Glan–Taylor polarizer) and a half-wave plate in the front of the integrated InGaAs detector. Near-infrared μ-PL measurement of strained TiS_3 was collected by a 50× infrared objective and fed to a spectrometer (LabRAM Odyssey, Horiba) equipped with a cryogenic InGaAs detector with a 532 nm laser for excitation.

3 Results and discussion

A top view of the atomic structure of TiS_3 is shown in Fig. 1(a). Ti atom is encompassed by six sulfur atoms, forming bicapped distorted tetrahedrons. 1D chains are formed through strong covalent bonds along the crystallographic *b*-axis and these repeating 1D chains are covalently bonded within the *a*–*b* plane into a layered structure. The distorted in-plane crystal structure dictates its anisotropic optical and electronic properties. The layers are further stacked by weak van der Waals force with no dangling bonds out of the plane. The crystal structure of the experimentally grown TiS_3 was identified by X-ray diffraction (XRD), where the prominent diffraction peaks closely matched its crystal standard PDF card (PDF# 36-1337) [Fig. 1(b)]. The detailed atomic crystal structure and element composition characterization can

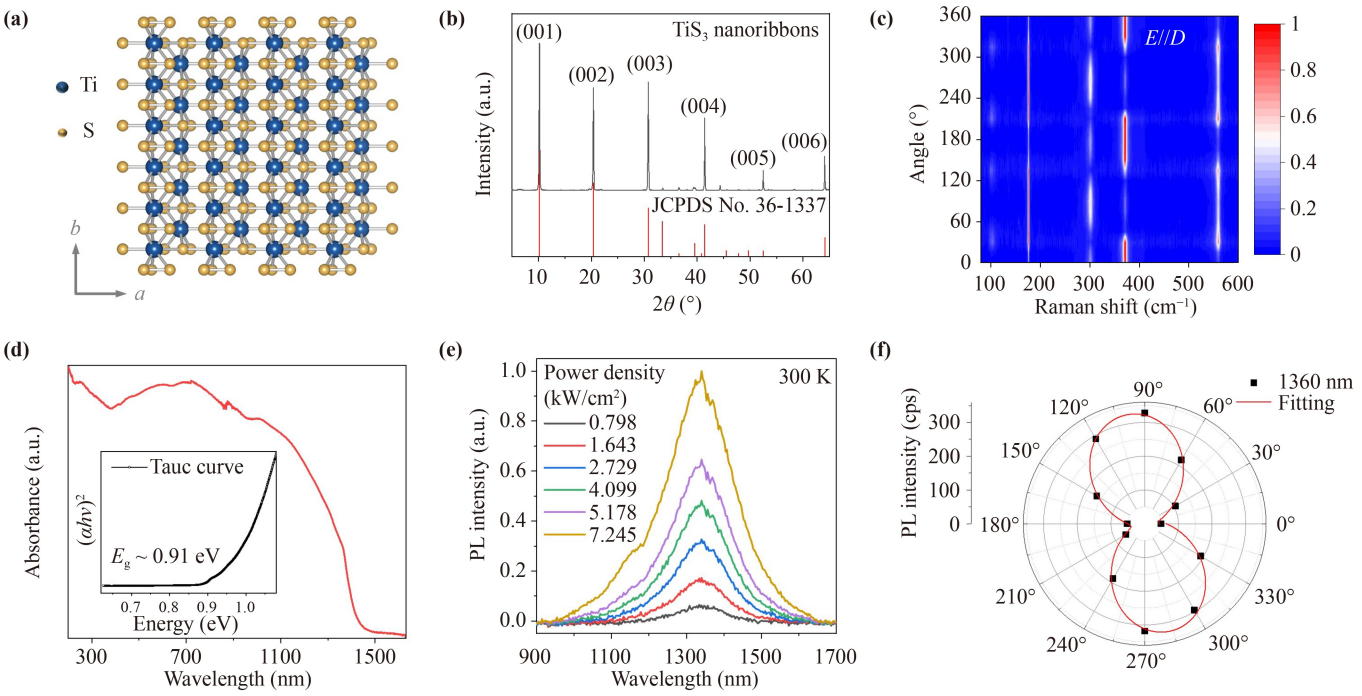

Fig. 1 Optical properties of quasi-1D TiS_3 nanoribbons. **(a)** Atomic structure model of TiS_3. **(b)** XRD patterns of the TiS_3 nanoribbons. **(c)** Polarized Raman intensity mapping of TiS_3 nanoribbon as a function of Raman shift and incident angle. Here the polarization direction of excitation (E) was parallel to the direction of detection (D). **(d)** UV-vis absorption spectrum of TiS_3 nanoribbon at room temperature, the inset is Tacu plot of TiS_3 nanoribbon extracted from the absorption spectrum. **(e)** Photoluminescence spectra of TiS_3 nanoribbon under various excitation powers at 300 K. **(f)** Polar plot of the polarized photoluminescence, cps: counts per second.

be seen in Fig. S1 of the electronic supplementary materials (ESM). The anisotropic lattice vibration of the TiS_3 nanoribbon was characterized by angle-resolved Raman spectroscopy in the parallel configuration, as shown in Fig. 1(c). Four Raman-active vibrational peaks at 175.9 cm^{-1}, 300.6 cm^{-1}, 371.3 cm^{-1} and 559.6 cm^{-1} were observed, corresponding to the out-of-plane vibrational peak I-A_g^{rigid}, in-plane vibrational mode II-$A_g^{internal}$ and III-$A_g^{internal}$, and in-plane S–S bond vibrational peak Ⅳ-A_g^{S-S}, respectively. We set the initial direction of the incident laser parallel to the b-axis (corresponding to 0°, as illustrated in Fig. S2 of the ESM) and the Raman intensity of different modes goes through maxima and minima with the variation of polarization angle with two- or four-lobed features, which can be explained from the Raman tensor analysis [32].

The Ultraviolet-Visable-Near infrared (UV-Vis-NIR) optical absorption of TiS_3 nanoribbons exhibits an absorption edge at around 1400 nm, as shown in Fig. 1(d). The inset shows the corresponding Tauc's plot, expressed as $(\alpha h\nu)^{1/n} = A(h\nu - E_g)$, where α, h, ν, A, and E_g are the absorption coefficient, Planck's constant, light frequency, proportionality constant, and band gap, respectively. We extracted n equals to 1/2 for TiS_3, which is consistent with its direct bandgap nature. The band gap of TiS_3 nanoribbon is estimated to be ~0.91 eV, which lies in the near-infrared O band region. The PL spectra of typical TiS_3 flakes at 300 K with various excitation powers are shown in Fig. 1(e). PL emissions at around 1330 nm were observed, which are in agreement with the absorption results, suggesting its radiative recombination in the band edge. It is worth noting that the TiS_3 flakes show stable PL emission under the excitation, as shown in Fig. S3 of the ESM. The PL spectra at 77 K (Fig. S4 of the ESM) show distinct PL signals of silicon substrate and TiS_3. With the decreasing of temperature, the PL intensity increases and the FWHM narrows, which could be attributed to the inhibited nonradiative recombination center at low temperatures. The ratio of the logarithm of the spectral integral PL to the logarithm of the excited power density (slope c) can be obtained to be ~0.9 at 77 K (Fig. S4 of the ESM), and this sub-linear dependence implies contribution from possible defect states [29]. Furthermore, Fig. 1(f) shows the linear polarization of the PL with a degree of polarization of about 77% and we elucidate that the polarization is along the b-axis (chain direction). Angle-resolved PL spectra of TiS_3 flake evolving with angle are shown in Fig. S5 of the ESM. Further, to clarify the stability of the sample, we examined the emission of the samples after two months in ambient conditions, and no degradation was observed, demonstrating its high environmental stability (Fig. S6 of the ESM).

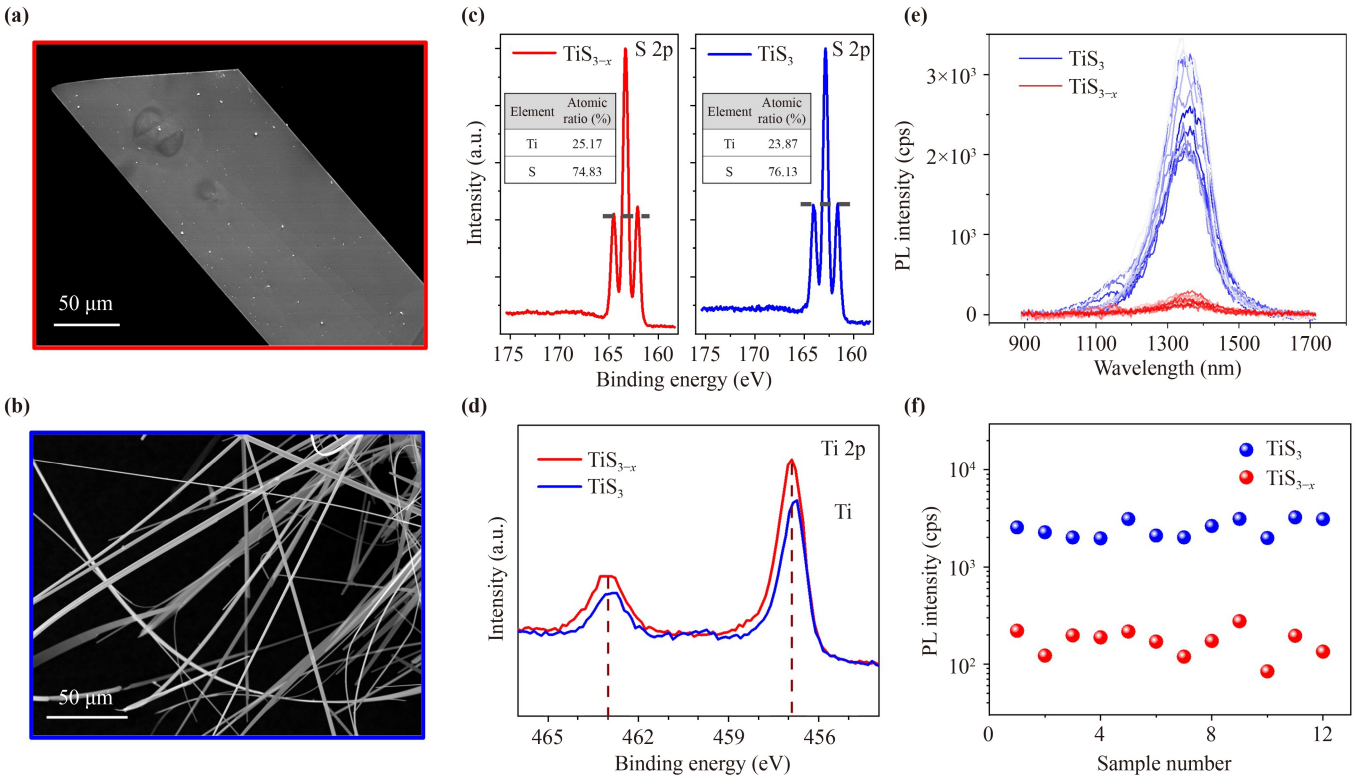

Fig. 2 Tune the PL emission intensity of TiS_3 nanoribbons by defect engineering. **(a)** The SEM image of TiS_{3-x}. **(b)** The SEM image of TiS_3. **(c, d)** High-resolution XPS spectra of S and Ti core level spectra of TiS_{3-x} and TiS_3, respectively. **(e, f)** PL spectra and intensity of TiS_{3-x} and TiS_3.

One significant challenge for layered TiS_3 is its sulfur vacancy introduced in the growth process, which would result in defect states and reduce the electron–hole radiative recombination rate [30, 31]. To increase the emission properties of the layered TiS_3, we explored the growth method for TiS_3 to effectively reduce the S vacancies. Different from the typical CVT growth with iodine granule as a transport agent, we used sulfur powder as a transport agent instead. Compared with TiS_{3-x} nanosheets grown with iodine granule as a transport agent [Fig. 2(a)], TiS_3 grown by S-self-transport has higher crystallinity and is more likely to grow into nanowires rather than nanosheets, as shown in the scanning electron microscope (SEM) image in Fig. 2(b). The fact that TiS_3 with a nanowire shape tends to have a lower density of sulfur vacancies is consistent with previous reports [28]. X-ray photoelectron spectroscopy (XPS) was employed to further verify the difference in sulfur vacancy content of TiS_3 and TiS_{3-x} nanoribbons. The S/Ti atomic ratios of TiS_3 and TiS_{3-x} were obtained to be 2.97 and 3.19 respectively, as shown in Fig. 2(c). In the S 2p spectra of TiS_3 and TiS_{3-x}, the S_2^{2-} peak decreases, as shown by the red curve in Fig. 2(c), which suggests the presence of more S_2^{2-} vacancies in TiS_{3-x}. In addition, a slight shift to lower binding energy was observed in the Ti 2p spectra from TiS_{3-x} to TiS_3 [Fig. 2(d)], which is consistent with the trend from TiS_2 to TiS_3 [30, 33–35]. More details of the XPS results are shown in Fig. S7 of the ESM. The reduction of S vacancies directly affects the near-infrared light emission of TiS_3, as shown in Fig. 2(e). Under the same excitation optical power density (532 nm, 0.798 kW/cm^2) and the identical detection configuration, TiS_3 (blue spectral curves) has a stronger PL than TiS_{3-x} (red spectral curves). The typical PL emission intensity of TiS_3 is an order of magnitude larger than TiS_{3-x} [Fig. 2(f)], demonstrating the effective regulation of infrared PL in TiS_3 by reducing the sulfur vacancies.

In addition to increasing the near-infrared PL intensity from 2D semiconductors, it is desired to control the wavelength of the emission, especially in optical communication applications. Firstly, taking advantage of the van der Waals interaction in the layered TiS_3, we explored its thickness-dependent luminescence. Figure 3(a) shows the normalized PL spectra of TiS_3 nanoribbons at room temperature with thicknesses from 16 to 261 nm (The thicknesses were determined by an atomic force microscope (AFM) in Fig. S8 of the ESM). As the thickness decreases, the center wavelength of the PL spectra shows blue shift and the band gap increases, which are attributed to the quantum confinement effect [36]. A summary of the bandgap variation with the number of layers is shown in Fig. 3(b), which decreases monotonously from 0.974 eV at 16 nm (~13 layers) to

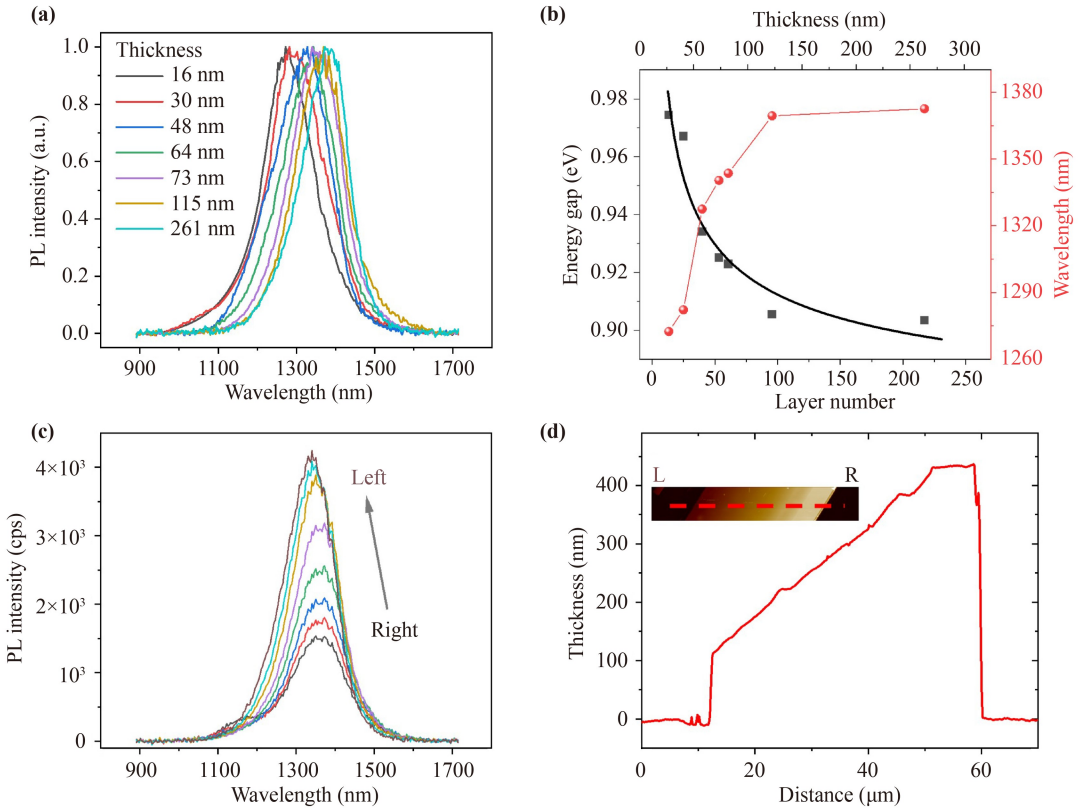

Fig. 3 PL emissions of TiS_3 nanoribbons by thickness regulation. **(a)** Thickness dependence of the PL spectra of TiS_3 nanoribbons. **(b)** Thickness dependence of TiS_3 band gap. **(c)** PL spectra of TiS_3 nanoribbons with a graded thickness. **(d)** The height profile of the thickness of the flake in (c) and the inset illustration is the AFM image.

0.903 eV at 261 nm thick TiS_3 nanoribbons (~217 layers). The optical bandgap is in good agreement with the experimental result obtained by scanning tunneling spectroscopy, photoelectrochemical measurements [37], and theoretical predictions [25, 38, 39]. In addition, the layer number dependent peak energy can be fitted by a one-dimensional tight-binding model [black curve of Fig. 3(b)] [40], $E = 0.345/N^{0.403}+0.858$, where E and N are band gap and layer number of TiS_3, respectively. We also observed the distinct emission wavelengths in TiS_3 nanoribbon with a thickness gradient, as shown in Fig. 3(c). The TiS_3 nanosheet with gradient thickness was exfoliated to the Si/SiO_2 substrate by the micromechanical cleavage technique. The optical diagram is shown in Fig. S9 of the ESM, and the corresponding height profile and AFM image are shown in Fig. 3(d). From the right side of the TiS_3 nanosheet to the left side, the thickness decreases gradually, and the corresponding center wavelength of PL spectra exhibits a blue shift. This is consistent with the previous results at different thicknesses. In short, by increasing the thickness of TiS_3, the central wavelength of the TiS_3 nanoribbons PL can vary from 1289 nm to 1342 nm. The emission range of TiS_3 (counting the range of full width at half maximum) spans from 1200 nm to 1460 nm covering the O and E bands, unlocking great potential for applications as gain materials in on-chip light sources.

Strain engineering is a powerful method to dynamically modulate the properties of 2D materials. We further apply tensile strain to dynamically modulate the emission wavelength of TiS_3 deposited on flexible substrates with a home-built strain setup, as shown in Fig. 4(a). Here, we use an elastomeric polyethylene terephthalate (PET) as a flexible substrate and encapsulate the TiS_3 nanoribbons with polymethyl methacrylate (PMMA) to ensure that strain is applied to the TiS_3 flakes [41, 42]. Tensile strain is calculated by $\varepsilon = \frac{d}{2R}$, where d and R are the thickness and radius of curvature of the flexible PET substrate, respectively. We further apply uniaxial tensile strain along the b-axis and a-axis of the TiS_3 to explore its anisotropic response [Fig. 4(a)]. When the strain is along the b-axis direction, the redshifts of the II-$A_g^{internal}$ and III-$A_g^{internal}$ modes are observed while the I-A_g^{rigid} and IV-A_g^{S-S} remain unchanged, as shown in Figs. 4(b) and S10 of the ESM. With strain of 0.096%, redshifts of ~2.01 cm^{-1} for the III-$A_g^{internal}$ mode and ~0.65 cm^{-1} for the II-$A_g^{internal}$ mode was observed. Raman modes soften with the tensile strain implying that the energy of the corresponding phonon modes decreases, thus weakening the associated restoring force in these vibrations. The Grüneisen parameter [γ_m, $\gamma_m = -\frac{1}{\omega_m}\frac{\Delta\omega_m}{\Delta\varepsilon}$, where ω_m =

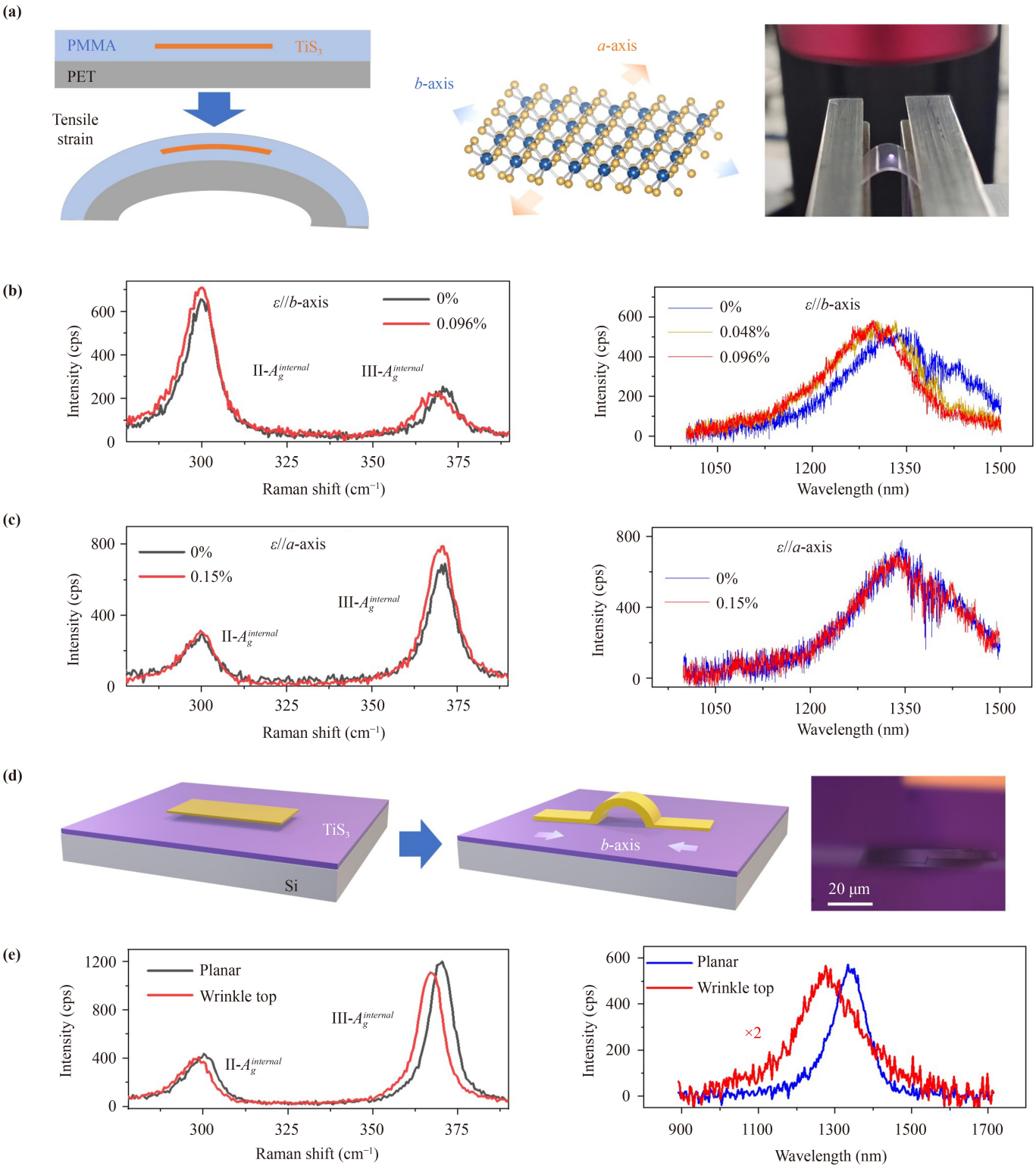

Fig. 4 Anisotropic response of PL spectra of TiS_3 nanoribbons under tensile strain. **(a)** Schematic diagram of the strain experiment and home-built setup. Strains are applied along the *a*-axis (perpendicular to the chain direction, orange arrow) and the *b*-axis (along the chain direction, blue arrow), respectively. **(b)** Raman and PL spectra of TiS_3 nanoribbon with the strain applied along the *b*-axis. **(c)** Raman and PL spectra of TiS_3 nanoribbon with the strain applied along the *a*-axis. **(d)** Schematic diagram of the existence of the wrinkle along the *b*-axis direction in TiS_3 nanoribbon. **(e)** Raman and PL spectra of the wrinkled TiS_3 nanoribbon.

370.48 cm^{-1}, $\Delta\varepsilon = \varepsilon_b - \upsilon\varepsilon_b$ (υ = 0.33 for PET)], which represents the shift rate of the active mode as lattice expanding, is 5.65 for III-$A_g^{internal}$, consistent with previous results [42]. Figure 4(b) also shows the PL spectra measured without strain (blue curve) and with strain (khaki and red curve) applied along the *b*-axis. A blueshift of PL spectra can be seen from 1338 nm to 1316 nm with 0.048% tensile strain, and as the tensile strain continues to increase to 0.096%, the center wavelength of the PL continues to blueshift to ~1289 nm. In contrast, when 0.15% strain is applied along *a*-axis, a slight redshift of the III-$A_g^{internal}$ Raman vibration peak was observed while the center wavelength of PL are almost unchanged [Fig. 4(c)]. The results show that the strain response along the *a*-axis is different from the strain response along the *b*-axis. The giant anisotropy reflected in strain response is due to the quasi-one-dimensional structure of TiS_3. When tensile strain is applied along the *b*-axis, the Ti-S covalent bond length will be elongated, which will change the lattice structure and lead to an enlarged band gap. Whereas chains are connected by weak forces in the direction perpendicular to the chain, the tensile strain along the *a*-axis leads to a less sensitive response reflected from the Raman and PL spectra. Another sample with a strain-tuned bandgap is shown in Fig. S11 of the ESM.

To further apply higher strain to the TiS_3 nanoribbons, we prepared TiS_3 nanoribbons with wrinkles under uniaxial strain along the *b*-axis on the Si/SiO_2 substrate by mechanical exfoliation and dry transfer technique, with the schematic diagram and the optical micrograph exhibited in Fig. 4(d). Figures 4(e) and S12 of the ESM demonstrate the Raman spectra measured on the planar region and the top of the wrinkle region for TiS_3. On the top of the wrinkle region, II-$A_g^{internal}$ and III-$A_g^{internal}$ modes show distinct redshifts of 2.4 cm^{-1} and 3.62 cm^{-1}, respectively. A larger Raman mode redshift compared to Fig. 4(b) implies a larger strain at this wrinkle. According to the γ_m value of 5.65 and the shift, the strain along the *b*-axis is around 0.26%. Figure 4(e) also shows the PL spectra measured on the planar region and on the top of the wrinkle region, where the PL spectrum on the top of the wrinkle (red curve) is blue-shifted by ~66 nm. The Raman and PL response of another TiS_3 nanosheet with the wrinkle under the uniaxial strain along the *b*-axis on the Si/SiO_2 substrate is shown in Fig. S13 of the ESM, in which a similar blue shift was observed on the top of the wrinkle.

4 Conclusion

In summary, we report on the tunable near-infrared light emission of layered TiS_3 nanoribbons. We developed a method to use sulfur as a transport agent to decrease the sulfur vacancy in the crystal and enhance its emission intensity. Further, PL emission from 1200 to 1370 nm in the near-infrared O band at 300 K was observed under the regulation of the thickness of the flakes. In addition, we demonstrated the emission wavelength tunability through uniaxial tensile strain by both the flexible substrates and flakes with wrinkles with interesting anisotropic strain response along the *b*-axis and *a*-axis. The enhanced PL intensity and broadband wavelength tunability in the near-infrared O band offer the prospect for intelligent integrated light sources for communication applications.

Declarations The authors declare that they have no competing interests and there are no conflicts.

Electronic supplementary materials The online version contains supplementary material available at https://doi.org/10.1007/s11467-023-1376-1 and https://journal.hep.com.cn/fop/EN/10.1007/s11467-023-1376-1.

Acknowledgements This work was supported by the National Key R&D Program of China (No. 2021YFA1200804), the National Natural Science Foundation of China (Grant Nos. 62274175, T2325025, and 61927813), Jiangsu Province Key R&D Program (Nos. BE2023009-5 and BE2021007-3), and the open Foundation of Key Laboratory of Nanodevices of Jiangsu Province (No. ZS2301). J. Wang acknowledges the support from the CAS Young Talent program under Grant No. E3291305. The authors are grateful for the technical support for the Vacuum Interconnected Nanotech Workstation (Nano-X) from Suzhou Institute of Nano-Tech and Nano-Bionics (SINANO), Chinese Academy of Sciences.

References

1. S. Famà, L. Colace, G. Masini, G. Assanto, and H. C. Luan, High performance germanium-on-silicon detectors for optical communications, *Appl. Phys. Lett.* 81(4), 586 (2002)
2. D. A. B. Miller, Device requirements for optical interconnects to silicon chips, *Proc. IEEE* 97(7), 1166 (2009)
3. A. Shacham, K. Bergman, and L. P. Carloni, Photonic networks-on-chip for future generations of chip multiprocessors, *IEEE Trans. Comput.* 57(9), 1246 (2008)
4. M. Streshinsky, R. Ding, Y. Liu, A. Novack, C. Galland, A. E. J. Lim, P. Guo-Qiang Lo, T. Baehr-Jones, and M. Hochberg, The road to affordable, large-scale silicon photonics, *Opt. Photonics News* 24(9), 32 (2013)
5. J. Yang, M. Tang, S. Chen, and H. Liu, From past to future: On-chip laser sources for photonic integrated circuits, *Light Sci. Appl.* 12(1), 16 (2023)
6. W. C. Yue, P. J. Yao, L. X. Xu, and H. Ming, All-dielectric bowtie waveguide with deep subwavelength mode confinement, *Front. Phys.* 13(4), 134207 (2018)
7. D. S. Liu, J. Wu, H. Xu, and Z. Wang, Emerging light-emitting materials for photonic integration, *Adv. Mater.* 33(4), 2003733 (2021)
8. J. You, Y. Luo, J. Yang, J. Zhang, K. Yin, K. Wei, X.

Zheng, and T. Jiang, Hybrid/integrated silicon photonics based on 2D materials in optical communication nanosystems, *Laser Photonics Rev.* 14(12), 2000239 (2020)
9. C. B. Qin, X. L. Liang, S. P. Han, G. F. Zhang, R. Y. Chen, J. Y. Hu, L. T. Xiao, and S. T. Jia, Giant enhancement of photoluminescence emission in monolayer WS_2 by femtosecond laser irradiation, *Front. Phys.* 16(1), 12501 (2021)
10. K. F. Mak, C. Lee, J. Hone, J. Shan, and T. F. Heinz, Atomically thin MoS_2: A new direct-gap semiconductor, *Phys. Rev. Lett.* 105(13), 136805 (2010)
11. R. S. Sundaram, M. Engel, A. Lombardo, R. Krupke, A. C. Ferrari, P. Avouris, and M. Steiner, Electroluminescence in single layer MoS_2, *Nano Lett.* 13(4), 1416 (2013)
12. D. H. Lien, S. Z. Uddin, M. Yeh, M. Amani, H. Kim, J. W. III Ager, E. Yablonovitch, and A. Javey, Electrical suppression of all nonradiative recombination pathways in monolayer semiconductors, *Science* 364(6439), 468 (2019)
13. M. Paur, A. J. Molina-Mendoza, R. Bratschitsch, K. Watanabe, T. Taniguchi, and T. Mueller, Electroluminescence from multi-particle exciton complexes in transition metal dichalcogenide semiconductors, *Nat. Commun.* 10(1), 1709 (2019)
14. S. Wang, J. Wang, W. Zhao, F. Giustiniano, L. Chu, I. Verzhbitskiy, J. Zhou Yong, and G. Eda, Efficient carrier-to-exciton conversion in field emission tunnel diodes based on MIS-type van der Waals heterostack, *Nano Lett.* 17(8), 5156 (2017)
15. J. Feng, Y. Li, J. Zhang, Y. Tang, H. Sun, L. Gan, and C. Z. Ning, Injection-free multiwavelength electroluminescence devices based on monolayer semiconductors driven by an alternating field, *Sci. Adv.* 8(5), eabl5134 (2022)
16. D. H. Lien, M. Amani, S. B. Desai, G. H. Ahn, K. Han, J. H. He, J. W. III Ager, M. C. Wu, and A. Javey, Large-area and bright pulsed electroluminescence in monolayer semiconductors, *Nat. Commun.* 9(1), 1229 (2018)
17. N. Gupta, H. Kim, N. S. Azar, S. Z. Uddin, D. H. Lien, K. B. Crozier, and A. Javey, Bright mid-wave infrared resonant-cavity light-emitting diodes based on black phosphorus, *Nano Lett.* 22(3), 1294 (2022)
18. N. Higashitarumizu, S. Tajima, J. Kim, M. Cai, and A. Javey, Long operating lifetime mid-infrared LEDs based on black phosphorus, *Nat. Commun.* 14(1), 4845 (2023)
19. Y. Wang, Q. Yu, J. Li, J. Wang, and K. Zhang, Insight into the growth mechanism of black phosphorus, *Front. Phys.* 18(4), 43603 (2023)
20. C. Ruppert, B. Aslan, and T. F. Heinz, Optical properties and band gap of single- and few-layer $MoTe_2$ crystals, *Nano Lett.* 14(11), 6231 (2014)
21. Y. Q. Bie, G. Grosso, M. Heuck, M. M. Furchi, Y. Cao, J. Zheng, D. Bunandar, E. Navarro-Moratalla, L. Zhou, D. K. Efetov, T. Taniguchi, K. Watanabe, J. Kong, D. Englund, and P. Jarillo-Herrero, A $MoTe_2$-based light-emitting diode and photodetector for silicon photonic integrated circuits, *Nat. Nanotechnol.* 12(12), 1124 (2017)
22. J. Yang, R. Xu, J. Pei, Y. W. Myint, F. Wang, Z. Wang, S. Zhang, Z. Yu, and Y. Lu, Optical tuning of exciton and trion emissions in monolayer phosphorene, *Light Sci. Appl.* 4(7), e312 (2015)
23. H. Shu, Highly-anisotropic carrier transport and optical properties of two-dimensional titanium trisulfide, *J. Mater. Sci.* 57(5), 3486 (2022)
24. Z. Lian, Z. Jiang, T. Wang, M. Blei, Y. Qin, M. Washington, T. M. Lu, S. Tongay, S. Zhang, and S. F. Shi, Anisotropic band structure of TiS_3 nanoribbon revealed by polarized photocurrent spectroscopy, *Appl. Phys. Lett.* 117(7), 073101 (2020)
25. J. Dai and X. C. Zeng, Titanium trisulfide monolayer: Theoretical prediction of a new direct-gap semiconductor with high and anisotropic carrier mobility, *Angew. Chem. Int. Ed.* 54(26), 7572 (2015)
26. Y. Jin, X. Li, and J. Yang, Single layer of MX_3 (M = Ti, Zr; X = S, Se, Te): A new platform for nano-electronics and optics, *Phys. Chem. Chem. Phys.* 17(28), 18665 (2015)
27. I. J. Ferrer, J. R. Ares, J. M. Clamagirand, M. Barawi, and C. Sánchez, Optical properties of titanium trisulphide (TiS_3) thin films, *Thin Solid Films* 535, 398 (2013)
28. J. O. Island, M. Barawi, R. Biele, A. Almazán, J. M. Clamagirand, J. R. Ares, C. Sánchez, H. S. J. van der Zant, J. V. Álvarez, R. D'Agosta, I. J. Ferrer, and A. Castellanos-Gomez, TiS_3 transistors with tailored morphology and electrical properties, *Adv. Mater.* 27(16), 2595 (2015)
29. A. Khatibi, R. H. Godiksen, S. B. Basuvalingam, D. Pellegrino, A. A. Bol, B. Shokri, and A. G. Curto, Anisotropic infrared light emission from quasi-1D layered TiS_3, *2D Mater.* 7(1), 015022 (2019)
30. Z. Tian, X. Guo, D. Wang, D. Sun, S. Zhang, K. Bu, W. Zhao, and F. Huang, Enhanced charge carrier lifetime of TiS_3 photoanode by introduction of S_2^{2-} vacancies for efficient photoelectrochemical hydrogen evolution, *Adv. Funct. Mater.* 30(21), 2001286 (2020)
31. Y. Wei, Z. Zhou, and R. Long, Defects slow down nonradiative electron–hole recombination in TiS_3 nanoribbons: A time-domain *ab initio* study, *J. Phys. Chem. Lett.* 8(18), 4522 (2017)
32. K. Wu, E. Torun, H. Sahin, B. Chen, X. Fan, A. Pant, D. Parsons Wright, T. Aoki, F. M. Peeters, E. Soignard, and S. Tongay, Unusual lattice vibration characteristics in whiskers of the pseudo-one-dimensional titanium trisulfide TiS_3, *Nat. Commun.* 7(1), 12952 (2016)
33. K. Endo, H. Ihara, K. Watanabe, and S. I. Gonda, XPS study of one-dimensional compounds: TiS_3, *J. Solid State Chem.* 44(2), 268 (1982)
34. A. S. Shkvarin, Y. M. Yarmoshenko, M. V. Yablonskikh, A. I. Merentsov, and A. N. Titov, An X-ray spectrscopy study of the electronic structure of TiS_3, *J. Struct. Chem.* 55(6), 1039 (2014)
35. M. E. Fleet, S. L. Harmer, X. Liu, and H. W. Nesbitt, Polarized X-ray absorption spectroscopy and XPS of TiS_3: S K- and Ti L-edge XANES and S and Ti 2p XPS, *Surf. Sci.* 584(2–3), 133 (2005)
36. X. L. Li, W. P. Han, J. B. Wu, X. F. Qiao, J. Zhang, and P. H. Tan, Layer-number dependent optical properties of 2D materials and their application for thickness

determination, *Adv. Funct. Mater.* 27(19), 1604468 (2017)

37. A. J. Molina-Mendoza, M. Barawi, R. Biele, E. Flores, J. R. Ares, C. Sánchez, G. Rubio-Bollinger, N. Agraït, R. D'Agosta, I. J. Ferrer, and A. Castellanos-Gomez, Electronic bandgap and exciton binding energy of layered semiconductor TiS_3, *Adv. Electron. Mater.* 1(9), 1500126 (2015)
38. A. H. Firouzkhani, M. Vaez-Zadeh, H. Jamnezhad, and M. Berahman, Electronic and optical properties of monolayer TiS_3: DFT calculation, *J. Optoelectron. Adv. Mater.* 22(11–12), 623 (2020)
39. J. Kang and L. W. Wang, Robust band gap of TiS_3 nanofilms, *Phys. Chem. Chem. Phys.* 18(22), 14805 (2016)
40. C. Chen, F. Chen, X. Chen, B. Deng, B. Eng, D. Jung, Q. Guo, S. Yuan, K. Watanabe, T. Taniguchi, M. L. Lee, and F. Xia, Bright mid-infrared photoluminescence from thin-film black phosphorus, *Nano Lett.* 19(3), 1488 (2019)
41. Y. Li, Z. Hu, S. Lin, S. K. Lai, W. Ji, and S. P. Lau, Giant anisotropic Raman response of encapsulated ultrathin black phosphorus by uniaxial strain, *Adv. Funct. Mater.* 27(19), 1600986 (2017)
42. J. K. Qin, H. L. Sun, T. Su, W. Zhao, L. Zhen, Y. Chai, and C. Y. Xu, Strain engineering of quasi-1D layered TiS_3 nanosheets toward giant anisotropic Raman and piezoresistance responses, *Appl. Phys. Lett.* 119(20), 201903 (2021)